

Journal of Materials Chemistry C

Accepted Manuscript



This is an *Accepted Manuscript*, which has been through the Royal Society of Chemistry peer review process and has been accepted for publication.

Accepted Manuscripts are published online shortly after acceptance, before technical editing, formatting and proof reading. Using this free service, authors can make their results available to the community, in citable form, before we publish the edited article. We will replace this *Accepted Manuscript* with the edited and formatted *Advance Article* as soon as it is available.

You can find more information about *Accepted Manuscripts* in the [Information for Authors](#).

Please note that technical editing may introduce minor changes to the text and/or graphics, which may alter content. The journal's standard [Terms & Conditions](#) and the [Ethical guidelines](#) still apply. In no event shall the Royal Society of Chemistry be held responsible for any errors or omissions in this *Accepted Manuscript* or any consequences arising from the use of any information it contains.

Hydrothermal preparation of WO₃ nanorod arrays and ZnO nanosheet arrays composite structures on FTO substrates with enhanced photocatalytic properties

Feng Zheng^{a,b,c}, Hui Lu^a, Min Guo^{*,a}, Mei Zhang^a, Qiang Zhen^{b,c}

Abstract: We reported a simple and effective hydrothermal route for fabricating WO₃ nanorod arrays (WNRs) and ZnO nanosheet arrays (ZNSs) composite structures on FTO substrate. The morphology evolution of the WNRs grown on FTO substrate and the ZNSs deposited on the WNRs were investigated by scanning electron microscopy (SEM), high resolution transmission electron microscopy (HRTEM) and X-ray diffraction (XRD). The growth mechanisms of well aligned WNRs and ZNSs were intensively studied. Moreover, the optical and photocatalytic properties of the WNRs-ZNSs composite structures were also examined.

^a State Key Laboratory of Advanced Metallurgy, School of Metallurgical and Ecological Engineering, University of Science and Technology Beijing, Beijing 100083, P. R. China

^b Materials Science and Engineering college, Shanghai University, Shanghai 200444, P. R. China

^c Nano-science and Nano-technology Research Center, School of Materials Science and Engineering, Shanghai University, Shanghai 200444, P.R. China

* E-mail: guomin@ustb.edu.cn, Fax: +86 10 62334926

1. Introduction

Over the past few decades, nano-sized semiconductor powders for use as photocatalysts have attracted great attention for their smaller sizes, large specific surface, and non-toxic side effect¹. However, the nanometer powder materials are not easy to recycle in waste water and it may cause secondary pollution. Orientation semiconductor nano-arrays grown on substrates can solve this challenge. ZnO exhibits a band gap of 3.3 eV and an electron affinity of 4.2 eV which can be considered to be a viable approach in photocatalysis². Till now, different morphologies of ZnO nano-arrays such as ZnO nanorod arrays³, nanowire arrays⁴, nanotube arrays⁵ and nanosheet arrays⁶ have been used for the decomposition of organic substances. However, due to the wide band gap, ZnO suffers as its light absorption which is limited to a small spectral. To extend the utilization over visible region in the solar spectrum, several attempts have been made to reduce the band gap of ZnO. Comprising of noble metals and ZnO nanocrystals have attracted noteworthy attention because the noble metals can produce the Schottky barrier⁷ and serve as scavengers for photogenerated electrons⁸, bringing visible light photoactivation and promoting interfacial electron-hole separation in the photocatalytic process. Therefore, Au⁹, Ag¹⁰ and Pt¹¹, etc are employed to modify ZnO for enhancing UV photocatalytic efficiency and visible light activities. Typically, preparing these noble metals is to coat the ZnO layer with metal nanoparticles on top, and this metal nanoparticle surface coverage reduces the surface area between ZnO and the liquid, which result in the decrease the area of the catalytically active sites¹².

Another way to enhance the photocatalytic activity is the combining other semiconductors with ZnO nanostructures, such as TiO₂¹³, SnO₂¹⁴, WO₃¹⁵, etc. the semiconductor/semiconductor composite structures could make the best use of reaction area and spectral range. However, ZnO/TiO₂ composite and ZnO/SnO₂ composite only work under UV irradiation due to the large band gaps of TiO₂ (3.2 eV)¹⁶ and SnO₂ (3.6 eV)¹⁷, leading to the restriction of their practical

applications. WO_3 is an indirect semiconductor with an adjustable band gap of 2.4-3.65 eV¹⁸⁻¹⁹ and can be used to couple with ZnO to broaden the spectral response range and retard photogenerated carrier recombination when it has a narrow band gap. Lam, et al.²⁰ synthesized WO_3 nanoparticles with an average size range of 18–26 nm coated on ZnO nanorods (ZNRs) by combining a hydrothermal technique with a chemical solution process. The WO_3 -ZNRs nanocomposites could be used in fluorescent-light photodegradation of endocrine disrupting chemicals such as phenol, bisphenol A and methylparaben. Xie, et al.²¹ prepared WO_3 -ZnO composites with different WO_3 contents via a simple aqueous solution route at 180 °C. The WO_3 -ZnO composites showed higher degradation efficiency under UV-Vis light compared with pure ZnO and P25. Very recently, Adhikari, et al.²² dispersed ZnO nanobelt to WO_3 nanocuboid by using physical mixing. The composite nanostructures were used to degrade cationic methylene blue and anionic orange G under visible light radiation. The high degree of 90% degradation of both dyes was due to the activity of the mixed oxides, which was much higher than that obtained either with WO_3 or ZnO individually. However, preparation of WO_3 -ZnO composite nanostructure arrays on substrate still remain challenge, and detailed studies on these issues are inadequate up to now. So, it is necessary to explore the conditions of preparing WO_3 -ZnO composite nanostructure arrays and their photocatalytic properties.

In this paper, we reported hydrothermal growth of a narrow band gap WO_3 nanorod arrays (WNRs) on FTO substrate and a wide band gap ZnO nanosheet arrays (ZNSs) on the WNRs. The morphology evolution and growth mechanism of WNRs and ZNSs were studied. Some optical properties such as UV-vis absorption spectra and photoluminescence spectra of the WNRs-ZNSs composite structures were systematically investigated. In addition, the photocatalytic property and mechanism of the WNRs-ZNSs composite nanostructure arrays was also discussed.

2. Experimental sections

2.1. Materials

All chemicals (Beijing Chemicals Reagent Company) were of analytical reagent grade and used without further purification. All the aqueous solutions were prepared using double distilled and ion-exchanged water. Fluorine doped Tin Oxide (FTO, 10-15 Ω/cm^2) glass plates were used as substrates and were cleaned by standard procedures prior to use.

2.2. Synthesis of WNRs

Preparation of H_2WO_4 colloid solution for coating substrates was described as follows: tungstic acid powder (H_2WO_4 , 0.01 mol) was dissolved into hydrogen peroxide solution (H_2O_2 , 20 mL, 30 wt %) to yield a homogeneous and stable colloid. Then the colloid solution was dropped onto $4.5 \times 1.0 \text{ cm}^2$ FTO substrate for spin-coating (KW-4A, made by Chinese Academy of Sciences) and annealing (SX₂-4-10, made by Tianjin Zhonghuan Experimental Furnace Co., Ltd.). The spin-coating processes were performed at 3000 rpm for 30 s and the annealing processes were heated at 500 °C. These processes were recycled for three times, both of the previous two annealing processes were performed for 10 min and the last time for 30 min. After these processes the FTO substrate covered with WO_3 seed layers was obtained.

The WNRs generally perpendicular to the substrate were fabricated by using a typical hydrothermal method. The precursor solution was prepared as follows: sodium tungstate dihydrate powder ($\text{Na}_2\text{WO}_4 \cdot 2\text{H}_2\text{O}$, 0.025 mol) was dissolved in distilled water (25 mL). Then the final pH value of the precursor solution was adjusted by the following two steps. Firstly, the pH value of the solution was acidified to 2.0 with hydrochloric acid (HCl, 2 mol/L) by magnetic stirring, and white precipitate was generated. Secondly, the solution was diluted to 250 mL and oxalic acid ($\text{H}_2\text{C}_2\text{O}_4$) was added to the mixture to adjust the final pH value to 2.4. After stirred for 30 min, 20 mL of the precursor solution was transferred into a 50 mL Teflon-lined autoclave and sodium chloride (NaCl,

5.0×10^{-3} mol) was added to it. Then the hydrothermal growth was carried out at 170 °C for 2 h in a sealed Teflon-lined autoclave by immersing the FTO substrate with the WO_3 seed layers in the precursor solution. After the reaction finished, the autoclave was cooled to room temperature naturally. Subsequently, the as-deposited substrate was rinsed repeatedly with deionized water and dried in air.

2.3. Synthesis of WNRs-ZNSs composite structures

Preparation of zinc acetate ($\text{Zn}(\text{CH}_3\text{COO})_2$) colloid solution for ZnO seed crystal was described as follows: 16.5 g zinc acetate and 4.5 mL Monoethanolamine ($\text{C}_2\text{H}_7\text{NO}$) were added into a beaker, then ethylene glycol monomethylether ($\text{C}_3\text{H}_8\text{O}_2$) was added until the total volume of the mixed solution reached as 100 mL. Then, the mixed solution was heated at 60 °C with stirring to form a homogeneous and stable colloid. Before hydrothermal growth, a ZnO seed layer was deposited onto the WNRs by dropping zinc acetate colloid solution on the WNRs and spin-coating. The WNRs with a layer of zinc acetate colloid were subsequently annealed at 300 °C for 10 min. After that, the WNRs covered with ZnO seed crystal were obtained.

The WO_3 -ZnO composite structures were synthesized by the following steps: 15 mL zinc nitrate ($\text{Zn}(\text{NO}_3)_2$, 0.1 mol/L) and 15 mL hexamethylenetetramine ($\text{C}_6\text{H}_{12}\text{N}_4$, 0.1 mol/L) were transferred into a 50 mL stainless steel Teflon-lined autoclave. After the WNRs with the ZnO seed layer were immersed into the reaction system, the autoclave were sealed and kept at 95 °C for 2 h in an oven. Then the autoclave was cooled to room temperature naturally. Subsequently, the as-deposited substrate was rinsed repeatedly with deionized water and dried in air.

2.4. Sample characterization

The X-ray diffraction (XRD) analysis was performed on a powder X-ray diffractometer (Rigaku Dmax-2500 diffractometer using $\text{Cu K}\alpha$ radiation). The morphologies of the nanostructures were observed on a field emission scanning electron microscope (FESEM, Zeiss, Supra-55) and high

resolution transmission electron microscope (HRTEM, Philips, Tecnai F20). The ultraviolet visible absorption spectrum was measured using UV-VIS-NIR recording spectrophotometer (Shimadzu, UV-3100). The Photoluminescence (PL) spectrum was excited by a He-Cd laser (IK Series) with a wavelength of 325 nm at room temperature.

2.5. Photocatalytic tests

The photocatalytic activities of the WNRs-ZNSs composite structures were evaluated through photodegradation of methylene blue (MB). The experiment was carried out in a 500 mL capacity photoreactor. To avoid the heating effect on the photocatalytic reaction, the photoreactor was kept at 25 °C by circulating cold water. The FTO substrates with the WNRs-ZNSs composite structures were added into the photoreactor containing 200 mL of 16 mg/L MB. The catalyst mass was 0.015 g calculated by the value of FTO substrates mass before and after hydrothermal reaction. The reaction mixtures were allowed to stand under dark conditions for 30 min to reach adsorption-desorption equilibrium of MB on the catalyst before light illumination. Then the reaction mixture was exposed directly to a 500 W xenon lamp. The concentrations of the solutions were monitored colorimetrically by using a UV-vis spectrophotometer (TU-1901, Beijing Purkinje General Instrument Co., Ltd.) in the spectral region between 400 and 800 nm.

3. Results and discussion

3.1. Preparation and characterization of primary WNRs on FTO substrate

The chemical reactions of deposition of WO_3 occurred in the hydrothermal process are as follows (eqn(1-2))²³:



The morphology of WNRs strongly depends on the deposition conditions, such as pH value, concentration of Na_2WO_4 , additive NaCl amount, temperature, reaction time in precursor solution

and substrate pre-treatment. By taking advantage of pre-modifying the substrates with WO_3 seed layers and appropriate parameters, such as optimum H^+ , WO_4^{2-} , NaCl concentration, temperature and reaction time, WNRs can be obtained.

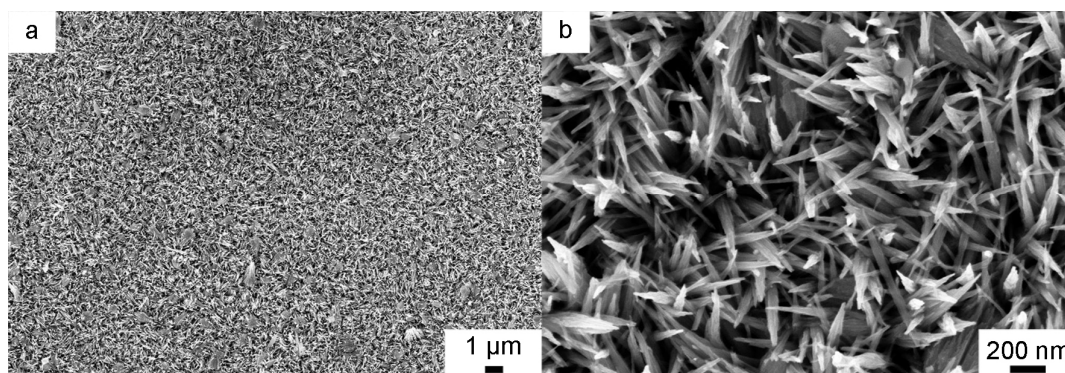


Fig. 1 SEM images of WNRs (a) with low magnification and (b) with high magnification.

Fig. 1 shows FESEM images of as synthesized WNRs at $170\text{ }^\circ\text{C}$ for 2 h. It can be seen from Fig. 1a that sharp cone-like WO_3 nanorods grow in large scale mixed with rare spindle-like nanorod bundles. The diameters of these nanorods are estimated from Fig. 1b to be about 100 ± 20 nm in width. X-ray diffraction (XRD) analysis is employed to investigate the crystal phases of the nanostructured materials. Fig. 2 shows the XRD pattern of the primary WNRs grown on FTO substrate, in which all the diffraction peaks can be well indexed to the standard diffraction pattern of hexagonal phase WO_3 (JCPDS 01-085-2460).

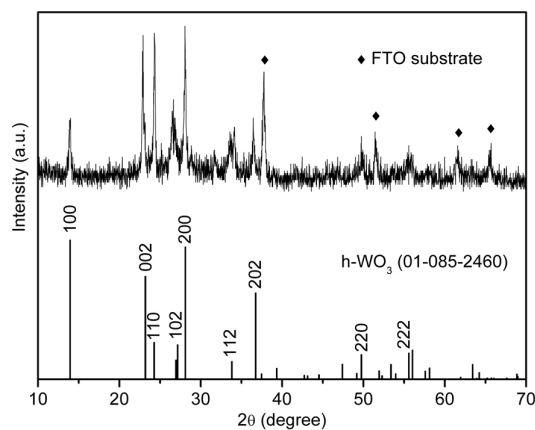


Fig. 2 X-ray diffraction (XRD) pattern of WNRs.

In order to study the growth mechanism of the primary WNRs on pre-coated FTO substrates, SEM images are taken at $170\text{ }^\circ\text{C}$ for different reaction time as shown in Fig. 3. It can be seen from

Fig. 3a that a smooth surface of the WO_3 seed layers is obtained before hydrothermal reaction. The orientation of the seeds can be divided into two kinds: parallel to substrate such as [200], [420] directions and non-parallel to substrate such as [202], [222] directions (Fig. S1). In our previous work²⁴, it has been demonstrated that h- WO_3 with growth direction along [001] is preferential to be formed during hydrothermal process ascribed to the anisotropy crystal growth and the role of NaCl as capping agent. Therefore, when hydrothermal reaction proceeds for 15 min, the surface of the seed layers becomes uneven, suggesting WO_3 nanoparticles in the seed layers begin to grow along c-axis as shown in Fig. 3b. With the time increasing to 30 min, some small white dots (WO_3 crystals) can be discerned on substrate (Fig. 3c). It is found that the WO_3 nanorods parallel and non-parallel to substrate both appear with time prolonging to 1 h in Fig. 3d. The angles between the [001] direction of formed nanorods and FTO substrate depend on the orientation of the seed layers. The nanorods grow independently because the average size of the seeds is small at the initial stage of hydrothermal reaction. Further prolonging the time to 1.5 h (Fig. 3e), the growth of nanorods parallel to substrate can be restrained by that non-parallel since no additional templates are used. When the growth time increases to 2 h, the formed nanorods can be arrayed and stand vertically to the substrate as the nanorods get denser and squeeze among each other as illustrated in Fig. 3f.

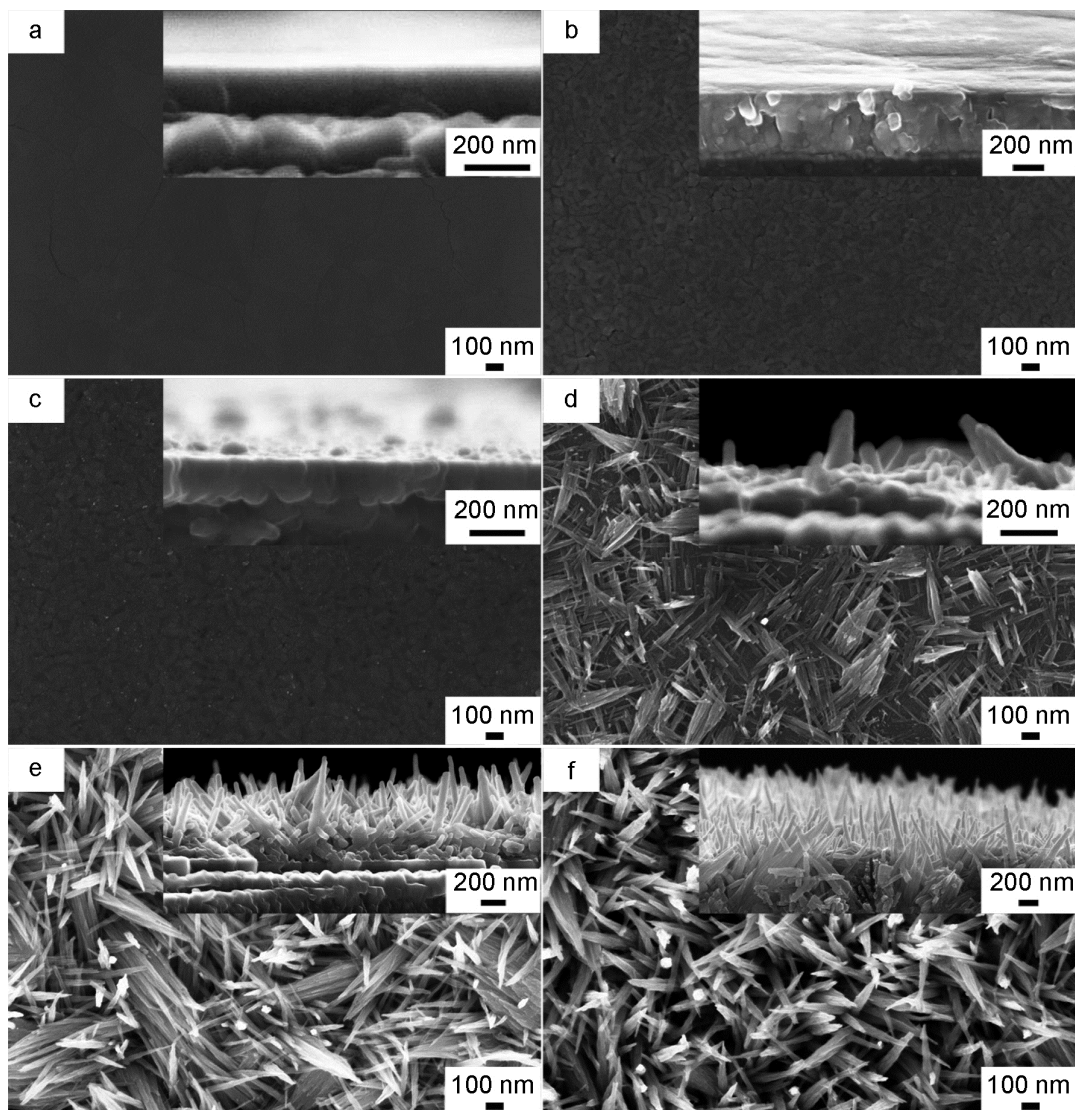


Fig. 3 SEM images of WO_3 nanostructures grown on FTO substrates at different hydrothermal reaction time. (a) 0 min, (b) 15 min, (c) 30 min, (d) 1 h, (e) 1.5 h, and (f) 2 h. Insets are the corresponding cross-sectional view images.

3.2. Preparation and characterization of WNRs-ZNSs composite structures on FTO substrate

Fig. 4a shows a typical FESEM image of as synthesized WNRs-ZNSs composite structures, where the ZNSs are uniformly distributed on the entire surface of WNRs. So, the WNRs cannot be seen clearly. As shown in Fig. 4b, the ZnO nanosheets are in fact hexagonal sheets with a diameter of several hundred nanometers and a width of few tens nanometers. Further information about WNRs-ZNSs composite structures is obtained from the EDX spectrum (Fig. 4c), indicating pure WO_3 and ZnO without any impurities are realized via hydrothermal process.

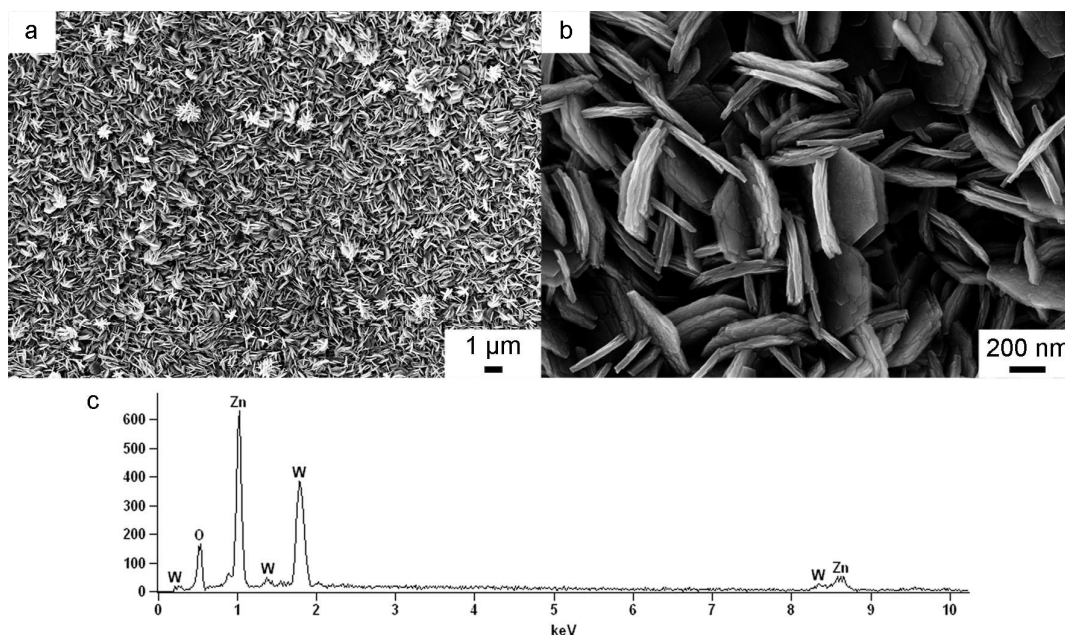


Fig. 4 SEM images of WNRs-ZNSs composite structures (a) with low magnification and (b) with high magnification. (c) EDX spectrum of WNRs-ZNSs composite structures.

To further study the growth mechanism of ZNSs on WNRs, SEM images are taken at 95 °C for different reaction time, as shown in Fig. 5 and Fig. 6. Fig. 5a and Fig. 6a give the morphologies of the primary structures - the WNRs. Compared with the primary structures, the WNRs are covered with a layer of ZnO nanoparticles after 60 min hydrothermal reaction time (Fig. 5b and Fig. 6b). With the time increasing to 70 min, as the moderate concentration existed in the precursor solution, the ZnO nuclei then grow to ZnO nanosheets by incorporating the residual ZnO species in the solution. Further prolonging the reaction time to 80-120 min, both the sizes and the number of the formed ZnO nanosheets become larger, thus, the nanosheets could be arrayed and stand vertically by squeezing amongst each other. In addition, the shape of the ZnO nanosheets turns to hexagon gradually as the hydrothermal reaction time increased. And the morphology of the WO₃ nanorods/ZnO nanosheets heterostructures could be adjusted by hydrothermal reaction time (Fig. S2).

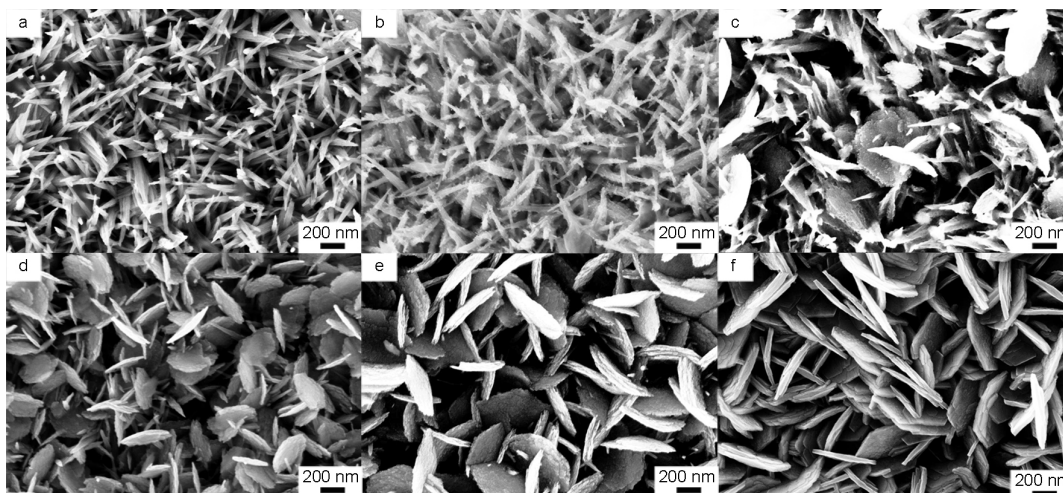


Fig. 5 SEM images of the ZnO nanosheets grown on WNRs for different hydrothermal reaction time. (a) 0 min, (b) 60 min, (c) 70 min, (d) 80 min, (e) 90 min, and (f) 120 min.

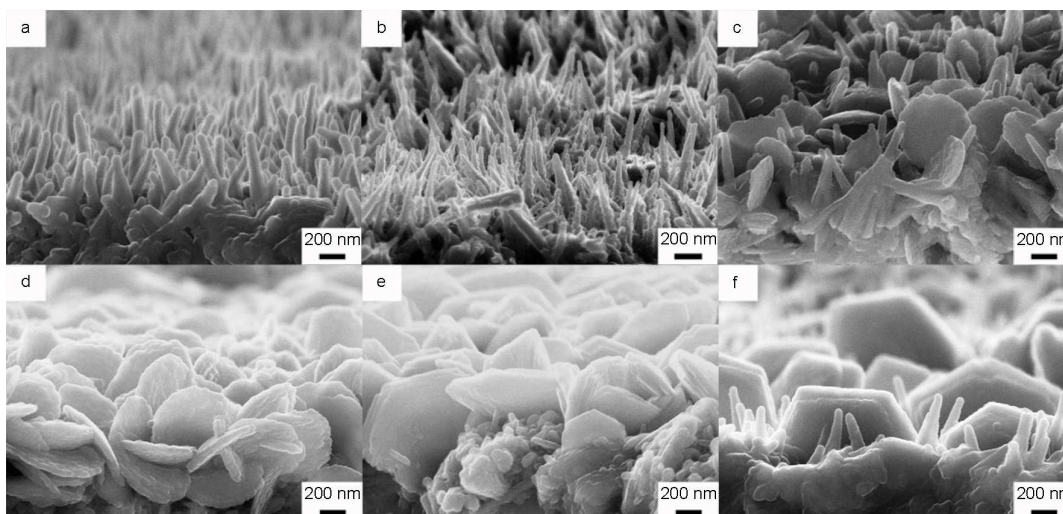


Fig. 6 Cross-sectional view SEM images of the ZnO nanosheets grown on WNRs for different hydrothermal reaction time. (a) 0 min, (b) 60 min, (c) 70 min, (d) 80 min, (e) 90 min, and (f) 120 min.

Fig. 7 shows the XRD patterns of the ZnO nanosheets grown on WNRs for different hydrothermal reaction time. The characteristic diffraction peaks of hexagonal WO_3 (01-085-2460) appear in all the samples. Comparing Fig. 7 b, c, and d with Fig. 7 a, it is found that the (001) plane diffraction peaks of the WNRs almost disappear. In our previous work²⁵, it is confirmed that the WNRs tend to grow along [001] direction, so the top face of the WNRs with smaller area is (001) crystal plane, which can be easily covered by ZnO nanosheets. In addition, relatively lower hexagonal ZnO (01-074-0534) diffraction peaks can also be observed and the intensity of the

diffraction peaks change little with the hydrothermal reaction proceeding, indicating the crystallinity of the grown ZnO is lower compared with that of the WNRs.

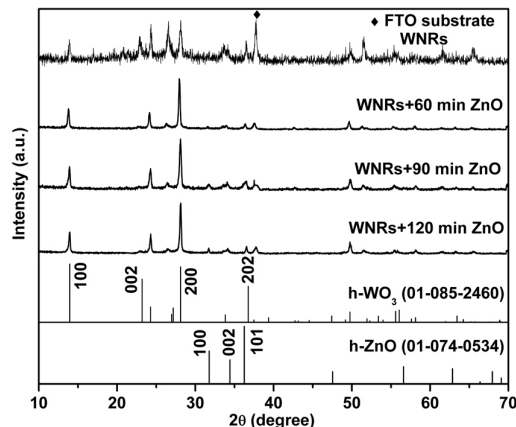


Fig. 7 XRD patterns of the ZnO nanosheets grown on WNRs for different hydrothermal reaction time. (a) 0 min, (b) 60 min, (c) 90 min, and (d) 120 min.

Fig. 8a shows the HRTEM images of WO₃ nanorod and ZnO nanosheet arrays composite structures. It can be seen that the spacing of the lattice fringes of the nanorod are about 0.383 nm and 0.317 nm, which can be well indexed as the (002) and (200) planes of hexagonal structure WO₃ (JCPDS: 01-085-2460). And the spacing of the lattice fringes of the nanosheet are about 0.247 nm and 0.260 nm, which are consistent with the (101) and (002) planes of hexagonal structure ZnO (JCPDS: 01-074-0534). From Fig. 8a, many ZnO nanosheets grow on the WO₃ nanorod, indicating that the composite structures are heterostructures. In addition, more detail of morphological and structural features of ZnO nanosheets are shown in Fig. 8b and c. HRTEM and selected area electron diffraction (SAED) results show that the ZnO nanosheet is a single crystal and the nanosheet is parallel to (010) plane.

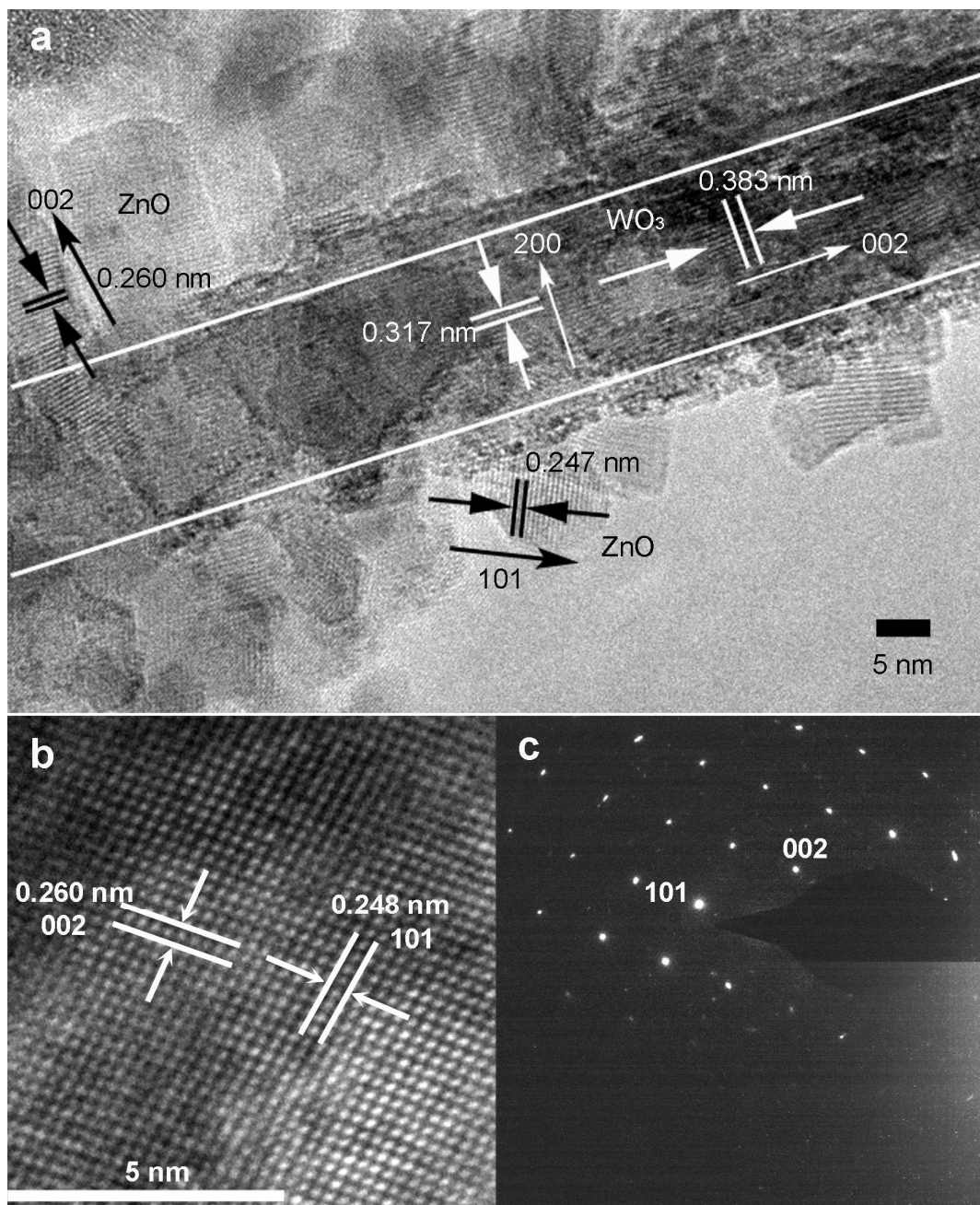


Fig. 8 (a) HRTEM images of WO_3 nanorod and ZnO nanosheet arrays composite structures. (b) HRTEM image of the ZnO nanosheet. (c) The selected area electron diffraction (SAED) pattern of the ZnO nanosheet.

According to the results of the SEM, TEM images and XRD patterns of the ZnO nanosheets, the formation mechanism of ZnO nanosheets grown on the WNRs can be explained by the well-known theory for crystal nucleation and growth. The chemical reactions occurred during the ZnO crystal nucleation and growth stages are as follows (eqn(3-6))²⁶:





It is well known that heterogeneous nucleation is easier than homogeneous nucleation, so, heterogeneous nucleation will take place preferentially on substrates in the precursor solutions. When the hydrothermal reaction begins (at the first stage), nucleation starts and the ZnO crystal nuclei can be firstly and preferentially formed on the surfaces of WNRs when the temperature exceeds the decomposition temperature of $\text{Zn}(\text{OH})_2$ ($34\text{ }^\circ\text{C}$)²⁷. With the hydrothermal reaction proceeding (at the second stage), the initial formed ZnO nuclei will grow with regular orientation, which may be caused by the anisotropy crystal growth of ZnO itself, the preferential adsorption of surfactants and the substrate effects. Usually, the ZnO nuclei will grow into nanorods on FTO substrate as shown in Fig. S3 under the hydrothermal conditions mentioned in the experimental (section 2.3). However, in this experiment, the primary WNRs substrate plays the key role in the formation of ZnO nanosheets. The WNRs grow along [001] direction and the spacing of the lattice fringes is about 0.383 nm. For hexagonal ZnO, the maximum spacing of the lattice fringes is 0.281 nm, which can be indexed as the (100) plane of JCPDS card (01-074-0534). The (100) plane is the same as (010) plane because of intrinsic symmetry of the hexagonal ZnO lattice. To satisfy the geometrical lattice matching, the ZnO crystal should grow parallel to the (010) planes and then form ZnO nanosheets. This can be verified by HRTEM images as indicated in Fig. 8. With the reaction time prolonging (at the third stage), the ZnO nanosheets act as “leader crystals” for the subsequent growth, both the density and the sizes of the formed nanosheets become denser and larger, leading to the formation of well aligned ZNSs on the WNRs since no additional templates are used in the formation process.

3.3. Optical properties of WNRs-ZNSs composite structures

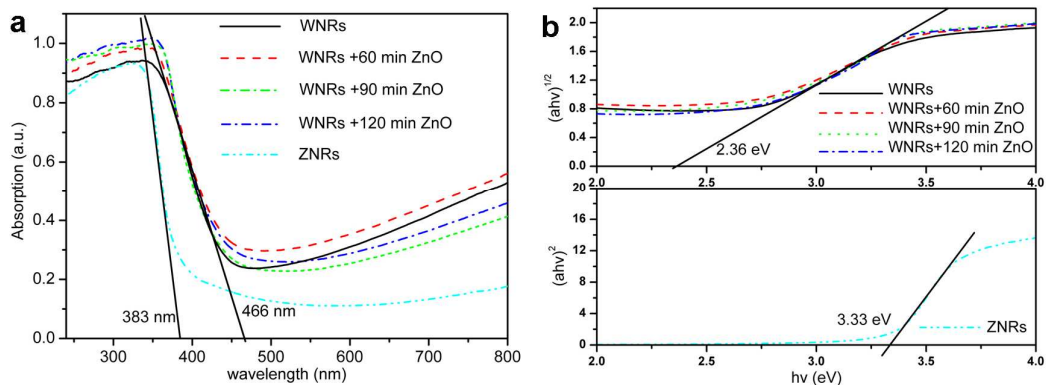


Fig. 9 (a) UV-vis absorption spectra of the ZNRs and ZnO nanosheets grown on WNRs for different hydrothermal reaction time. (b) $(ah\nu)^{1/2}$ (for indirect bandgap semiconductor) and $(ah\nu)^2$ (for direct bandgap semiconductor) are plotted as a function of $h\nu$ from which the band gap energies are obtained by a Tauc plot.

Fig. 9a shows the UV-visible absorption spectra of the ZNRs (Fig. S3) and ZnO nanosheets grown on WNRs for different hydrothermal reaction time. As for ZNRs, the absorption region is below 383 nm. However, as for the ZnO nanosheets grown on WNRs, the absorption region could be widened to 466 nm and enters the visible range. The band gap energies of the ZNRs and WO_3 -ZnO composite structures are calculated to be 3.33 eV and 2.36 eV as shown in Fig. 9b, respectively, according to the equation $ah\nu = A(h\nu - E_G)^n$, where E_G (eV) is band gap energy of the semiconductor, h is Planck's constant, ν is the frequency of light, A is a constant and the n has the value 0.5 for ZnO and 2 for WO_3 ²⁸. The results show that the WO_3 could extend spectrum absorption area, thus increase the utilization of visible light no matter how many ZnO exist in the WO_3 -ZnO composite structures.

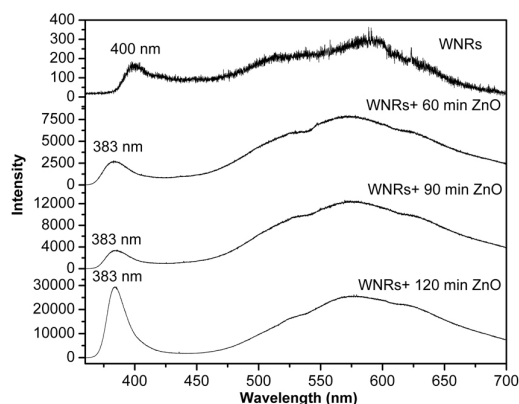


Fig. 10 The photoluminescence spectra of the WNRs and the ZnO nanosheets grown on WNRs for different hydrothermal reaction time.

The photoluminescence (PL) spectra are useful to reveal the efficiency of charge carrier trapping, migration and transfer so as to understand the fate of electrons and holes in the semiconductor since PL results from the recombination of free carriers²⁹. To further investigate the influence of hydrothermal reaction time on the optical properties of the WO₃-ZnO composite structures, PL measurements are conducted at room temperature as illustrated in Fig. 10. It can be seen that all of the PL spectra exhibited two obvious emission bands, including the ultraviolet emission band resulted from the near band-edge transition, and a strong and broad visible emission band originated from the intrinsic defects. For WNRs, the emission peaks appear at 400 nm and a yellow-green emission area is obtained from 450 to 650 nm. The emission peak at 400 nm is caused by the near band-edge transition, while the yellow-green area between 450 and 650 nm might be formed by oxygen vacancy and tungsten gap. When the ZnO is deposited on the WNRs, the near band-edge transition peak appeared at 383 nm which is a little blue shifted related to the band gap energies in Fig. 9a. Similarly to the WNRs, the yellow-green area between 500 and 700 nm might be formed by oxygen vacancy and zinc vacancy. With the hydrothermal reaction time increasing, the mass of the ZnO increases gradually, and the PL intensity increases greatly. This is because ZnO is a direct band gap semiconductor which could easily create pairs of electrons and holes. In addition, the band-edge PL intensity increases greatly compared with the visible PL intensity,

suggesting relatively longer hydrothermal reaction time may lead to formation of ZnO nanosheets with high crystallinity degree, and this phenomenon is consistent with the SEM images shown in Fig. 5 and Fig. 6.

3.4. Photocatalytic properties of WNRs-ZNSs composite structures

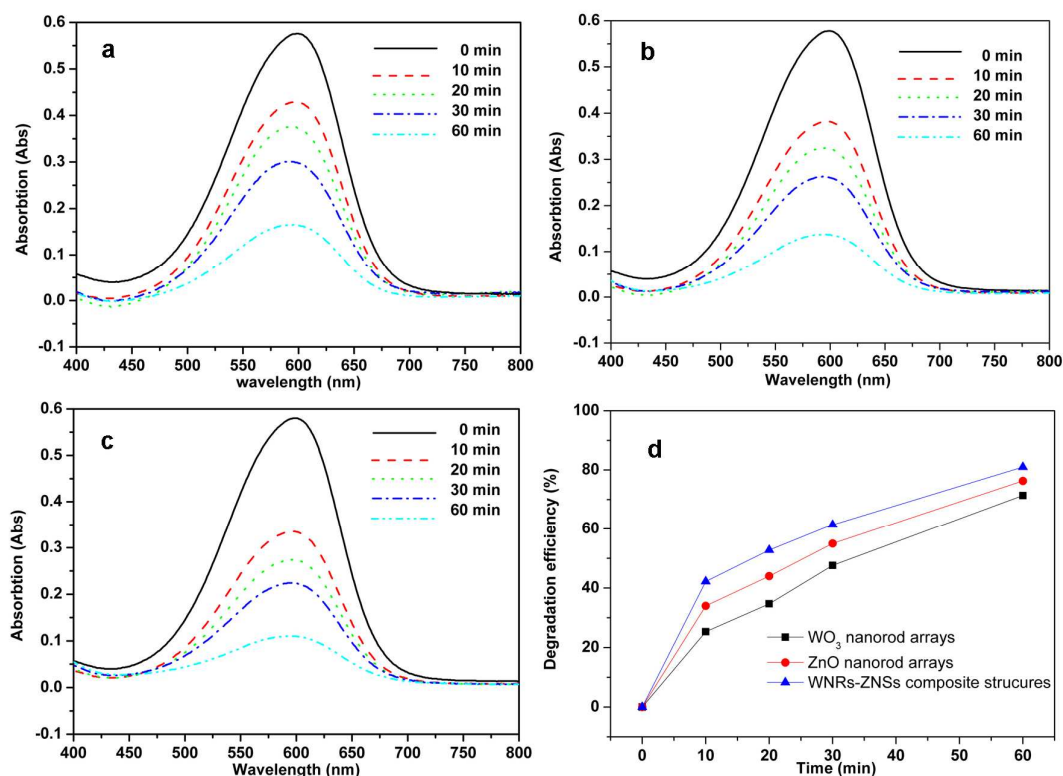


Fig. 11 The plots of absorption vs time of methyl blue solution photo degraded by (a) WNRs, (b) ZNRs, and (c) WNRs-ZNSs composite structures. (d) The photo catalytic degradation curve of methyl blue solutions with WNRs, ZNRs, and WNRs-ZNSs composite structures.

The degradation of methyl blue (MB) in the presence of WNRs, ZNRs, and WNRs-ZNSs composite structures are carried out and the absorbance changes of MB over time are displayed in Fig. 11 a-c. It is shown that the absorbances are reduced from 0.580 to 0.164 Abs for WNRs, 0.137 Abs for ZNRs, and 0.108 Abs for WNRs-ZNSs composite structures in 60 min, respectively. The absorbance of MB means the concentration of MB according to Lambert-Beer's law³⁰ which is gradually decreased with the WNRs as the catalyst. The ZNRs show a relatively high photocatalytic activity than the WNRs, which may be because that ZnO is a direct band gap semiconductor and

could produce large amounts of electron-hole pairs whereas the WO_3 is an indirect one. For WNRs-ZNSs composite structures, after 10 min irradiation under the visible light, about 42% of MB is sharply degraded. The photocatalytic degradation curves of MB solution (Fig. 11d) are calculated according to the equation $a=(A_0-A_t)/A_0$, where a is the degradation efficiency of MB, A_t is the absorbance of MB at the wavelength of 600 nm at time t and A_0 is the absorbance after the adsorption equilibrium on the samples prior to irradiation³¹. From Fig. 11, it can be clearly seen that the final degradation efficiency of the WNRs-ZNSs composite structures is higher than that of the WNRs or ZNSs individually.

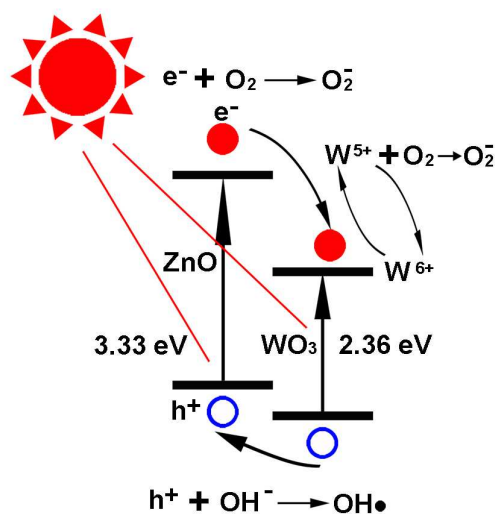


Fig. 12 The photocatalysis schematic diagram of WNRs-ZNSs composite structures.

The reasons why the WNRs-ZNSs composite structures have higher degradation efficiency could be explained as follows: Firstly, the WNRs-ZNSs heterostructures grown on FTO substrate distribute uniformly on large scales which can extend the photochemical reaction area. In fact, the FTO substrate is a glass covered with a layer of fluorine doped tin oxide. The tin oxide thin film is also a kind of semiconductor material which can be used as photocatalyst for degradation of dye³². In addition, the FTO substrate is transparent, which makes the sunlight irradiate the semiconductor nanostructures from all angles, so, the WNRs-ZNSs composite structures grown on FTO substrate can make full use of the sunlight. Secondly, the ZnO and WO_3 semiconductors can generate pairs

of electrons and holes (eqn(7))³³ under the illumination of ultraviolet and visible light. Then the photoelectrons can react with the adsorbed O₂ to produce superoxide radical anions (O₂⁻) (eqn(8)), and the holes can react with H₂O to produce hydroxyl radicals (OH•) (eqn(9)). Both the superoxide radical anions and hydroxyl radicals are responsible for the degradation of MB (eqn(10) and eqn(11))³⁴. Fig. S4 further illustrates the active OH• and O₂⁻ play important roles in photocatalytic degradation. For the WNRs-ZNSs composite structures, the ZnO nanosheets can create a large number of electron-hole pairs as a direct band gap semiconductor and WO₃ nanorods can absorb the visible light as a narrow gap semiconductor. The WNRs-ZNSs heterostructures can efficiently utilize sunlight.



Thirdly, the ZnO nanosheets and WO₃ nanorods are in close contact with each other, and both of the two nanostructures are single crystal, facilitating the photogenerated electrons and holes transfer from one semiconductor to the other. Fig. 12 shows the photocatalysis schematic diagram of WNRs-ZNSs composite structures for degradation of organic matter. The photogenerated holes transfer could occur from the valence band (VB) of WO₃ to the VB of ZnO, and in the meantime, the photogenerated electrons transfer could take place from the conduction band (CB) of ZnO to the CB of WO₃ since the conduct band position and valence band position of WO₃ are lower than that of ZnO³⁵. When electrons get trapped by WO₃, W⁶⁺ ions react with electrons immediately to form

W^{5+} , resulting the WO_3 act as a container to promote the separation of photoelectrons from vacancies. The W^{5+} ions on the surface of WO_3 are reoxidized to W^{6+} by oxygen that is subsequently reduced into O_2^{-36} . Therefore, the photodegradation efficiency can be enhanced by preventing the recombination rate of electrons and holes due to the efficient charge separation.

4. Conclusions

In summary, WNRs and ZNSs composite structures have been firstly prepared on FTO substrate by using a hydrothermal method. The formation mechanism of the WNRs and the ZNSs are reasonably deduced on the basis of study on the growth process of WNRs-ZNSs composite structures. The UV-visible absorption spectra show that the band gap energies of the ZnO and WO_3 are 3.33 eV and 2.36 eV, respectively. The photoluminescence spectra are consistent with the UV-visible absorption spectra. The results of photocatalytic degradation of MB indicate that the WNRs-ZNSs composite structures have higher degradation efficiency than that of the WNRs or ZNRs individually, which are mainly attributed to the wide absorption region of the solar energy and efficient charge separation between ZnO nanosheets and WO_3 nanorods.

Acknowledgment

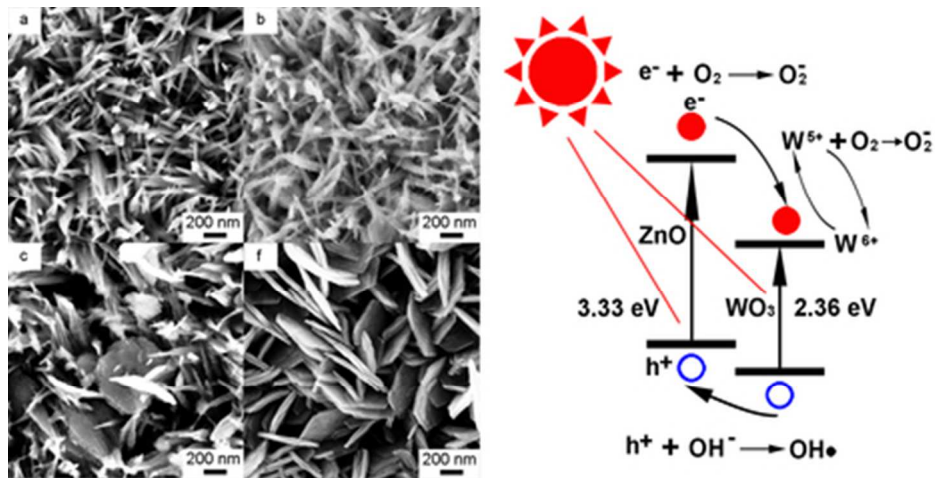
The work is supported by the National Nature Science Foundation of China (No. 51272025, 50872011, 50672006 and 51272154).

References

- 1 M. M. Khin, A. S. Nair, V. J. Babu, R. Murugan and S. Ramakrishna, *Energy Environ. Sci.*, 2012, 5, 8075-8109.
- 2 C. Mondal, J. Pal, M. Ganguly, A. K. Sinha, J. Jana and T. Pal, *New J. Chem.*, 2014, 38,

- 2999-3005.
- 3 D. Iqbal, A. Kostka, A. Bashir, A. Sarfraz, Y. Chen, A. D. Wieck and A. Erbe, *ACS Appl. Mater. Interfaces*, 2014, 6, 18728-18734.
 - 4 Y. C. Chang, *Catal. Commun.*, 2014, 56, 45-49.
 - 5 W. C. Lee, Y. Fang, R. Kler, G. E. Canciani, T. C. Draper, Z. T. Y. Al-Abdullah, S. M. Alfadul, C. C. Perry, H. He, Q. Chen, *Mater. Chem. Phys.*, 2015, 149-150, 12-16.
 - 6 H. Lu, S. Wang, L. Zhao, J. Li, B. Dong and Z. Xu, *J. Mater. Chem.*, 2011, 21, 4228-4234.
 - 7 Z. D. Meng, L. Zhu, J. G. Choi, M. L. Chen and W. C. Oh, *J. Mater. Chem.*, 2011, 21, 7596-7603.
 - 8 Q. Huang, T. Gao, F. Niu, D. Chen, Z. Chen, L. Qin, X. Sun, Y. Huang and K. Shu, *Superlattice Microst.*, 2014, 75, 890-900.
 - 9 X. Hou, *Mater. Lett.*, 2015, 140, 39-42.
 - 10 Y. Liang, N. Guo, L. Li, R. Li, G. Ji and S. Gan, *Appl. Surf. Sci.*, 2015, 332, 32-39.
 - 11 C. Yang, Q. Zhu, T. Lei and C. Xie, *J. Mater. Chem. C*, 2014, 2, 9467-9477.
 - 12 W. Smith and Y. Zhao, *J. Phys. Chem. C*, 2008, 112, 19635-19641.
 - 13 T. J. Athauda, J. G. Neff, L. Sutherlin, U. Butt and R. R. Ozer, *ACS Appl. Mater. Interfaces*, 2012, 4, 6917-6926.
 - 14 X. Huang, L. Shang, S. Chen, J. Xia, X. Qi, X. Wang, T. Zhang and X. M. Meng, *Nanoscale*, 2013, 5, 3828-3833.
 - 15 C. Yu, K. Yang, Q. Shu, J. C. Yu, F. Cao and X. Li, *Chin. J. Catal.*, 2011, 32, 555-565.
 - 16 A. Ayati, A. Ahmadpour, F. F. Bamoharram, B. Tanhaei, M. Manttari, M. Lahtinen, M. Sillanpaa, *Sep. Purif. Technol.*, 2014, 133, 415-420.
 - 17 J. T. Park, C. S. Lee and J. H. Kim, *RSC Adv.*, 2014, 4, 31452-31461.
 - 18 Z. Meng, A. Fujii, T. Hashishin, N. Wada, T. Sanada, J. Tamaki, K. Kojima, H. Haneoka and T.

- Suzuki, *J. Mater. Chem. C*, 2015, 3, 1134-1141.
- 19 I. Turyan, U.O. Krasovec and B. Orel, *Adv. Mater.*, 2000, 12, 330-333.
- 20 S. M. Lam, J. C. Sin, A. Z. Abdullah, A. R. Mohamed, *Ceram. Int.*, 2013, 39, 2343–2352.
- 21 J. Xie, Z. Zhou, Y. Lian, Y. Hao, X. Liu, M. Li and Y. Wei, *Ceram. Int.*, 2014, 40, 12519–12524.
- 22 S. Adhikari, D. Sarkar and G. Madras, *RSC Adv.*, 2015,5, 11895-11904.
- 23 J. Wang, E. Khoo, P. S. Lee and J. Ma, *J. Phys. Chem. C*, 2008, 112, 14306–14312.
- 24 F. Zheng, M. Zhang and M. Guo, *Thin Solid Films*, 2013, 534, 45-53.
- 25 F. Zheng, M. Guo and M. Zhang, *CrystEngComm*, 2013, 15, 277-284.
- 26 Y. Sun, J. Riley and M. N. R. Ashfold, *J. Phys. Chem. B*, 2006, 110, 15186-15192.
- 27 A. Goux, T. Pauporte, J. Chivot and D. Lincot, *Electrochim. Acta*, 2005, 50, 2239-2248.
- 28 J. Su, X. Feng, J. D. Sloppy, L. Guo and C. A. Grimes, *Nano Lett.*, 2011, 11, 203-208.
- 29 K. Mahmood, S. B. Park and H. J. Sung, *J. Mater. Chem. C*, 2013, 1, 3138-3149.
- 30 X. Wang, S. Zhou and L. Wu, *J. Mater. Chem. C*, 2013, 1, 7547-7553.
- 31 D. M. Tobaldi, R. A. S. Ferreira, R. C. Pullar, M. P. Seabra, L. D. Carlos and J. A. Labrincha, *J. Mater. Chem. C*, 2015, 3, 4970-4986.
- 32 A. Kar and A. Patra, *J. Mater. Chem. C*, 2014, 2, 6706-6722.
- 33 N. Huo, S. Yang, Z. Wei and J. Li, *J. Mater. Chem. C*, 2013, 1, 3999-4007.
- 34 L. Pan, X. Liu, Z. Sun and C. Q. Sun, *J. Mater. Chem. A*, 2013, 1, 8299-8326.
- 35 A. Hagfeldt and M. Gratzel, *Chem. Rev.*, 1995, 95, 49-68.
- 36 L. Zhang, Y. Li, Q. Zhang and H. Wang, *CrystEngComm*, 2013, 15, 5986-5993.



Textual abstract: Growth process of ZnO nanosheet arrays (ZNSs) on WO₃ nanorod arrays (ZNRs) and the photocatalysis schematic diagram of WNRs-ZNSs composite structures.
39x19mm (300 x 300 DPI)